Corrosion Science 154 (2019) 36–48

Contents lists available at ScienceDirect

Corrosion Science

journal homepage: www.elsevier.com/locate/corsci

Effect of tempering heat treatment on the CO_2 corrosion resistance of quench-hardened Cr-Mo low-alloy steels for oil and gas applications

Clara. Escrivà-Cerdán[a], Steve W. Ooi[b], Gaurav R. Joshi[a,*], Roberto Morana[c], H.K.D.H. Bhadeshia[b], Robert. Akid[a]

[a] School of Materials, The University of Manchester, Manchester, M13 9PL, United Kingdom
[b] Department of Materials Science & Metallurgy, University of Cambridge, Cambridge, CB3 0FS, United Kingdom
[c] BP Exploration Operating Company Limited, Chertsey Road, Sunbury-on-Thames, TW16 7LN, United Kingdom

ARTICLE INFO

Keywords:
Low alloy steel
Intermetallics
EIS
SEM
Interfaces

ABSTRACT

The corrosion resistances of a number of tempered states of two Cr-Mo low-alloy steels, the novel "HT10" (martensitic) and the commercial ASTM A182 grade "F22" (bainitic), were evaluated in CO_2-saturated brine. The tempering heat treatments soften both steels, due to a decrease in dislocation density, and the precipitation of alloy carbides, but also decrease their uniform corrosion rates. Such a decrease is considerable if the steels are tempered at higher temperature for longer time. For the novel HT10, we discuss how the tempering-induced changes to the microstructure contribute to decreasing the cathodic reaction kinetics, and thus the general corrosion rate.

1. Introduction

As the oil and gas industry seeks out deepwater resources, new low-alloy steels are required to cope with extreme temperatures, pressures, solution chemistries and mechanical stresses [1]. Although structural criteria such as strength and toughness are emphasised during component design, these steels must have an acceptable resistance to general and localised corrosion [2], whilst retaining their integrity against hydrogen embrittlement [3]. One of the most predominant forms of corrosion encountered during oil and gas production is caused by the action of dissolved CO_2, in water-containing hydrocarbon fluids, on the internal surfaces of steel components [4,5]. The general CO_2 corrosion resistance of carbon/low-alloy steel is a function of its composition, thermo-mechanical history and resulting microstructure, as addressed in Refs [6–9]. For a given composition, the nature of the microstructure (e.g. bainite, ferrite-pearlite), its stress state, corrosion scaling response and the shape, size and distribution of the primary carbide phase cementite (Fe_3C) are typically what determine uniform steel corrosion in CO_2 media [6–9]. Dispersed cementite, for instance, is suggested to create microscopic galvanic cells with the iron matrix throughout the microstructure, modifying the interfacial redox corrosion kinetics [10].

Regardless, mitigation strategies against CO_2 corrosion of steel in oil and gas applications most often comprise appropriate material selection [11,12], and corrosion inhibition practices [13,14]. Low-carbon steels with appropriate corrosion inhibition is a common approach, although the problematic scale formation on steel surfaces, during production, can influence the efficiency of chemical corrosion inhibitors [14]. Since corrosion resistant alloys are prohibitively expensive, the use of low-carbon steels with minor Cr additions (1–5 wt%) is an attractive proposition to minimise the CO_2 corrosion threat [15–20], with greater resistance afforded by a higher Cr content [16–18]. The resistance against corrosion is attributed to the formation and retention of a thin Cr-enriched film at the alloy/electrolyte interface [21–33]. One such Cr-containing low carbon steel, "F22" (ASTM A182), typically containing 2–2.5 wt% Cr, is used widely for forged components in a "quenched and tempered" heat-treated state. Although F22 can be heat-treated for higher strength, its susceptibility to failure by hydrogen embrittlement, arising from corrosion or external cathodic protection of the component, may then also be increased [3]. As such, a requirement of an 'economically-viable' high-strength low-alloy steel for oil and gas components, having adequate toughness and improved resistance to hydrogen embrittlement over conventional steels, has driven the design and development of a new Ni-Cr-V-Mo steel designated "HT10" [34,35]. This martensitic steel is intrinsically strong after austenitation and quenching, but its good toughness is obtained only after an appropriate tempering[1] heat treatment, as discussed in Ref. [34].

* Corresponding author.
E-mail address: Gauroba@gmail.com (G.R. Joshi).

[1] An annealing heat treatment, after austenitisation, in the range 400°C - 650°C) [58], typically for 1-10h.

https://doi.org/10.1016/j.corsci.2019.03.036
Received 30 September 2018; Received in revised form 5 February 2019; Accepted 21 March 2019
Available online 26 March 2019
0010-938X/

Having previously evaluated the tensile strengths and Charpy impact toughness of HT10, after a variety of tempering heat treatments [34], one important property left to assess is corrosion resistance. In this paper, we report on the corrosion performance of HT10 in the same quench-hardened and tempered states used in Ref. [34], against the "benchmark" of the widely used F22. In doing so, we address a specific gap in the literature on comparing the CO_2 corrosion performance of a variety of slightly different tempered states of the same quench-hardened Cr-Mo low-alloy steels. To achieve this, we use the electrochemical methods of open circuit potentiometry (V_{oc}), potentiodynamic polarisation and electrochemical impedance spectroscopy (EIS) to measure the corrosion response in CO_2-saturated simulated oilfield brine at 60 °C (pH = 5.4, P_{total} = 1 atm). Complementary substrate characterisation, through scanning electron microscopy (SEM) for imaging and energy dispersive X-ray spectroscopy (EDX) analysis, as well as metallurgical characterisation data included from partner studies of the same research programme [34,35], are what support the discussion concerning the acquired electrochemical corrosion data.

2. Experimental procedure

2.1. Materials

Chemical compositions of HT10 and F22 steels are presented in Table 1. The alloying content in both materials is similar, although HT10 contains additional Ni to improve its low temperature toughness, and higher V and Mo content to encourage alloy carbide precipitation (in favour of cementite). As outlined in Ref. [34], alloy HT10 is a secondary hardening alloy, i.e. one where the base material is austenitised, quenched and tempered to produce (Mo,V,Cr)-rich carbide precipitates dispersed throughout the microstructure [36]. In addition to the resulting grain structure, it is the dispersion of these precipitates that is expected to provide HT10 with improvements to its tensile strength and hydrogen trapping capacity [36]. In the current work, HT10 and F22 samples were provided for corrosion studies after a variety of quench and temper heat-treatments as detailed in Table 2. The F22 alloys are described using the key '*F22 - temper heat temperature/time*'; the HT10 alloys are described using the key '*A1 or A2*' (corresponding to the specific length of austenitation time at 850 °C) - *temper heat temperature/time*. For instance, an F22 alloy tempered at 700 °C for 3.5 h is described as 'F22-700 °C/3.5 h; an HT10 alloy austenitised at 850 °C for 5.8 h, before being water quenched (WQ) and tempered for 10 h is labelled 'A2-625 °C/10 h'.

2.2. Methods

Material hardness measurements were determined using a Struers Duramin-600 Vickers hardness tester applying a 30-kg load. For each heat treatment, 5–8 hardness indentations were made at random locations on 2–3 separate material surfaces (ground to 600 grit SiC), from which average hardness values and standard deviation errors were determined.

The corrosion performance of HT10 and F22, as a function of immersion time, was evaluated in CO_2-saturated simulated oilfield brine (see Table 3 for electrolyte composition) using electrochemical measurements. For this purpose, a 3-electrode setup was employed, using the HT10 or F22 steel sample as the working-electrode, a platinum flag as the counter-electrode and a saturated calomel electrode (SCE) as the reference-electrode. Experiments were carried out on individual working electrodes with a surface area of between1 - 1.6 cm^2 exposed to the test electrolyte; all remaining faces and edges were covered with an epoxy resin. The surface of the steel working electrode was abraded with wet SiC paper of increasing grit size (240–4000), followed by rinsing with deionised water/ethanol and drying in a stream of nitrogen gas (99.99% purity N_2 gas was used throughout this work, supplied by the company BOC). For images of the polished substrates prior to immersion, the reader is referred to Fig. A1 in the Supplementary Materials.

All electrochemical measurements were performed on samples immersed in a jacketed glass cell located within a nitrogen glove box, using a Solartron Modulab 2100 A potentiostat. The simulated oilfield brine (1 dm^3) contained in the cell was kept at a constant temperature (60 °C ± 2 °C) by circulating heated water through the cell's jacket. The solution was bubbled with CO_2 gas (99.95% purity, from BOC) for a period of 18 h. For further information on electrolyte preparation, details are available in Ref. [37].

Once ready, the electrolyte pH was measured (always found to be 5.4 (± 0.1), and an HT10 or F22 steel working-electrode sample was introduced and left to corrode at its open circuit potential (V_{oc}) vs. SCE for a period of 30 h. For each heat-treated variant, the corrosion behaviour was evaluated from open circuit potentiometry and hourly electrochemical impedance spectroscopy measurements (100 kHz - 50 mHz, ± 10 mV vs. V_{oc}). At the end of experiment, the electrode was removed from the brine, allowed to dry in the glove box's nitrogen atmosphere, and stored in a vacuum desiccator prior to SEM examination in a Quanta 250 FEG-SEM. The electrolyte pH was measured, and typically found to be 5.4 (± 0.1). After initial investigations of the surface, the corrosion products were removed from the surface using Clarke's solution, as per ASTM G1-03 [38]. Subsequently, sample surfaces were re-examined using SEM to probe for any localised corrosion morphology. All 30 h immersion experiments were conducted 2–3 times for each alloy variant, from which standard deviation errors were obtained.

For potentiodynamic polarisation measurements on the same materials, the working-electrodes of which were not used in 30 h immersion tests, the potential was scanned from -0.25 V (vs. V_{oc}) to +0.35 V (vs. V_{oc}) at a scan rate of 0.167 mV s^{-1} after ~15 min of immersion at V_{oc}. These types of tests were conducted twice for each alloy variant. The resulting polarisation curves were used to understand the anodic/cathodic reaction kinetics of the steels in the CO_2–sat. brine, by relying on the principles of fundamental electrochemical corrosion kinetics [39–41].

2.3. Calculations

Charge transfer resistances (R_{ct}) from impedance data modelling [42] (fitted using the in-built Solartron EIS software) along with the Stern-Geary coefficient (B parameter) from polarisation curves were used to estimate corrosion current density (I_{corr}) using Eqs. (1)–(3), i.e.

$$B = (\beta_a \beta_c)/2.303\,(\beta_a + \beta_c) \quad (1)$$

$$B_{diff\ control} = (\beta_a)/2.303 \quad (2)$$

$$I_{corr}\ (A/cm^2) = B/R_{ct} \quad (3)$$

Here, β_a and β_c are the anodic and cathodic Tafel slopes respectively (V $decade^{-1}$), and were examined for each alloy variant from the polarisation curves. It is emphasised that Eq. (1) strictly applies for activation-controlled kinetics, and Eq. (2) may be used to provide an estimate in the case of diffusion-controlled cathodic kinetics [43], where β_c is considered to be infinity. From I_{corr}, corrosion rates (CR) were determined using Eq. (4).

$$CR\ (mm/y) = (10^6 I_{corr}\ K\ E_w) / \rho \quad (4)$$

Table 1
Measured chemical composition (wt%) of HT10 and F22.

Alloy	C	Mn	Cr	Ni	Mo	V	Fe
F22	0.12	0.35	2.20	–	0.93	–	Balance
HT10	0.12	0.57	2.47	3.20	1.52	0.46	Balance

Table 2
Heat treatment regimes applied to the F22 and HT10 steels.

F22	HT10[a]	HT10[b]
920 °C followed by WQ	850 °C (for 3.5 h) followed by WQ	850 °C (for 5.8 h) followed by WQ
F22WQ	**A1-WQ**	**A2-WQ**
920 °C followed by WQ	850 °C followed by WQ	850 °C followed by WQ
Tempered at 580 °C for 4 h30 min.	Tempered at 600 °C for 1 h	Tempered at 625 °C for 1 h
F22-580 °C/4.5 h	**A1-600 °C/1 h**	**A2-625 °C/1 h**
900-980 °C followed by WQ	850 °C followed by WQ	850 °C followed by WQ
Tempered at 690-720 °C for 2.5-4.5 h followed by AC	Tempered at 600 °C for 10 h	Tempered at 625 °C for 10 h
F22-700 °C/3.5 h	**A1-600 °C/10 h**	**A2-625 °C/10 h**
–	850 °C followed by WQ	850 °C followed by WQ
	Tempered at 600 °C for 24 h	Tempered at 625 °C for 24 h
	A1-600 °C/24 h	**A2-625 °C/24 h**

WQ, water-quenched: AC is air-cooled. Sample codes given in bold.
[a] A1 is short austenitising time (3.5 h).
[b] A2 is a longer austenitising time (5.8 h).

Table 3
Chemical composition (C) of simulated oilfield brine used in corrosion experiments.

Ion	Na^+	K^+	Ca^{2+}	Mg^{2+}	Sr^{2+}	Cl^-	HCO_3^-	CH_3COO^-
C / $mg{\cdot}L^{-1}$	34829	195	2100	280	138	57280	465	1300

Here, CR is corrosion rate (mm/year), I_{corr} is corrosion current density (A/cm^2), K = material specific constant (3.27×10^{-3} for Fe), E_w is the equivalent weight per electron transferred in grams/equivalent (27.92) and ρ is the material density (7.86 g/cm^3).

3. Results

3.1. Material hardness

The influence of tempering temperature and time on F22 and HT10 hardness is shown in Fig. 1. The Vickers hardness decreases from a post-quench value of ~ 360 HV_{30} dependent upon tempering temperature and time. Rather consistent with the literature [44,45], we note that it is the tempering temperature that has a more profound effect on decreasing steel hardness. For instance, the decrease in HT10 hardness after 10 h tempering at 625 °C (decrease from 361 to 265 HV_{30}, loss of 35%), is considerably greater than after tempering for the same period of time at 600 °C (from 361 to 315 HV_{30}, loss of 12%). Indeed, the tempering of water-quenched F22 for ~4 h ± 0.5 h at 700 °C softens the steel to a far greater extent than a temper at 580 °C for a similar time exposure.

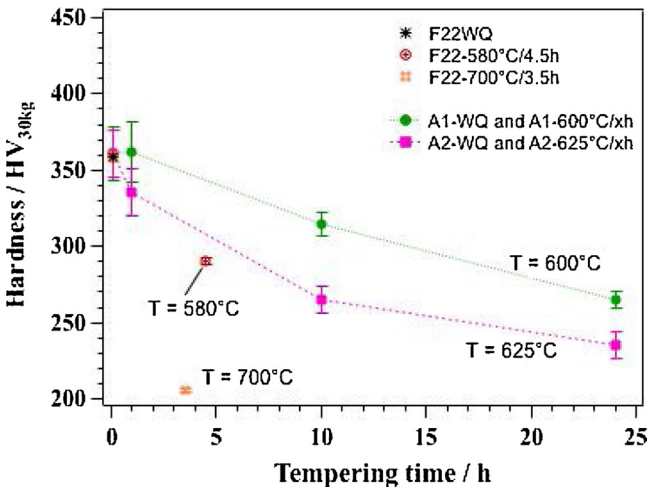

Fig. 1. Hardness (HV30) vs. tempering time (h) showing the influence of tempering conditions on the hardness of F22 and HT10.

3.2. Material microstructures

Example SEM micrographs (after 2% Nital etching) for as-quenched and quenched and tempered (Q&T) F22, and Q&T HT10 are provided in Fig. 2. The quench-hardened F22 (Fig. 2(a), F22WQ) presents a bainitic microstructure, with elongated cementite (Fe_3C) precipitates. A Q&T F22 (Fig. 2(b)), F22-700 °C/3.5 h) shows a tempered bainite microstructure with dispersed Fe_3C in the matrix; spherical Fe_3C precipitates are observed within, and in between, the ferrite plates.

Representative microstructures of two different Q&T heat treatments applied to HT10 are presented in Fig. 2(c–d). Both show tempered martensite, comprising dispersed precipitates, whose nature and chemistry using transmission electron microscopy and synchrotron X-ray diffraction are confirmed elsewhere [34,35]. The larger spherical precipitates are $_{\gamma}$MC type (M = V,Mo,Cr) that form *during austenitisation* at 850 °C, while the finer precipitates are a distribution of $_{\alpha}$MC (V-rich) and $_{\alpha}M_2C$ (Mo-rich) type that develop *during tempering*. Note: a smaller number of larger, spherical γMC-type precipitates (i.e. those formed during austenitisation) were identified in the HT10 A2-625 °C microstructures, and the converse in A1-600 °C. The key difference between these two variants is that' A2′ HT10 alloy samples were austenitised at 850 °C for 5.8 h, whereas' A1′ HT10 samples were austenitised at the same temperature for only 3.5 h. All the carbide precipitates were observed within martensite laths and at lath/grain boundaries, and appear well distributed throughout the microstructure. For more details on precipitate characteristics, the reader is referred to [34,35].

3.3. Electrochemical immersion: Polarisation curves in CO_2-sat. Brine (60 °C)

Fig. 3(a) show potentiodynamic polarisation curves taken from variants of HT10, as well as F22-580 °C/4.5 h. The general shapes for all polarisation curves appear similar, with an activation-controlled and pre-passivation regime evident in the anodic reaction domain (right side) and a diffusion-controlled regime observed in the cathodic reaction domain (left side). Table 4 lists the parameters extracted from the analysis of polarisation curves. In order to elucidate the results further, the same data in Fig. 3(a) are re-plotted in Fig. 3(b) and (c) as a function of their overpotential. Focusing first on the anodic regime, we show that Tafel kinetics are permissible as a decade of linearity is obtained. The anodic curves appear similar and overlapping and their Tafel slopes span between 60–70 mV $decade^{-1}$, within an expected range for an adsorbed CO_2-assisted iron oxidation mechanism at this pH and temperature [46–48]. At higher positive overpotential, the slope tends towards 100–120 mV as we enter a pre-passivation range for these alloys

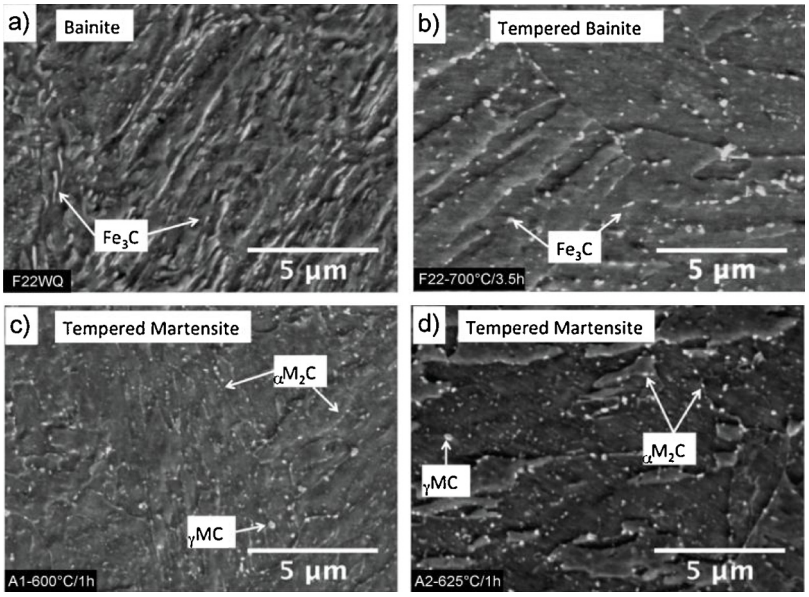

Fig. 2. SEM images of 2% Nital etched F22 steel (a) F22WQ (b) F22-700 °C/3.5 h, and HT10 steel (c) A1-600 °C/1 h and (d) A2-625 °C/1 h.

in this CO_2-saturated medium [48].

Considering the cathodic regime, we note that the anodic reverse reaction, the activation-controlled and mixed activation-diffusion controlled contributions are all contained within a very small 50 mV range away from the open circuit potential in these static electrolytes [49], and no linearity is obtained. Therefore, activation-controlled Tafel kinetics cannot apply. In a higher overpotential region (from -50 to -150 mV), as diffusion-controlled reaction kinetics become predominant, the cathodic curves shift slightly towards lower current density values as a function of tempering time. This is made clear in the magnified insets in Fig. 3(b–c). It suggests that those HT10 alloys that were tempered for longer tend to present a decrease in their cathodic reaction kinetics.

During polarisation curve analysis, I_{corr} values have been estimated from the intersection of the partial anodic and cathodic current density slopes presented in Fig. 3(b–c). The slopes in the cathodic overpotential range extend beyond 400 mV decade^{-1}, far higher than activation-controlled proton reduction (120 mV decade^{-1}) [49], and convey that the reaction mechanism comes under diffusion-control. Under a diffusion-limited current density, the mass transport of the participating electroactive species (e.g. CO_2(aq) and H^+(aq)) determines the corrosion reaction rate. In such a case, the corrosion current density is a function of the limiting current density of the cathodic partial reaction [50]. This is described in Eq. (5).

$$I_{corr} = I_{lim,\ c}\ (A/cm^2) = nFD(C_b)/\delta \quad (5)$$

Here, n = number of moles of electrons involved in the cathodic charge transfer reaction, F is the Faraday (96,485 C mol^{-1}), D is (are) the diffusion coefficient(s) of the electroactive species involved in the electrochemical reduction reaction (cm^2 s^{-1}), C_b is the bulk concentration of the electroactive species (mol), and δ is the thickness of the diffusion layer (cm). On the basis of this discussion, the B parameter to calculate corrosion rates is determined using Eq. (2), i.e assuming cathodic diffusion-controlled cathodic kinetics. Taken as an average from the anodic Tafel results presented in Table 4, the Eq. (2) calculation results in B = 28 mV decade^{-1}. We stress that our choice of the B coefficient does not impact upon the general corrosion trend as a function of tempering, which is the main focus of this study. An estimate of cathodic limiting current density ($I_{lim,c}$) at an overpotential of -0.125 V is also included in Table 4, to serve as a comparative basis of Q &T alloy performance later in the discussion.

3.4. Electrochemical immersion: 30 h exposures in CO_2-sat. Brine (60 °C)

3.4.1. Electrochemical impedance spectroscopy

Fig. 4(a–c) show Nyquist impedance plots of F22 and HT10 steels with different tempering times, respectively, after immersion in CO_2-sat. brine (T = 60 °C, pH = 5.4) for 30 h. Qualitatively, the impedance spectra from all F22 and HT10 alloy variants depict features that are more or less consistent with each other, and the relevant literature [23,31,51]. The Nyquist spectra in Fig. 4 consist of a depressed capacitive arc at high to medium frequencies (at low to medium Z') and a pseudo-inductive (or reverse capacitive) feature at lower frequencies (at high Z'). The capacitive arc could be considered to represent the interfacial capacitance, and is depressed due to frequency dispersion effects resulting from the heterogeneous nature of the corroding surface [52]; the pseudo-inductive arc at low frequencies is quite possibly due to the response associated with the adsorption of aqueous, electroactive reaction intermediates (e.g. ferrous hydroxide) involved in the corrosion of iron/steel [53–55]. The equivalent circuit model to fit all the data is presented in Fig. 4(d). In the equivalent circuit model, R_s (Ω cm^2) is the electrolyte solution resistance between the working and reference electrode, R_{ct} (Ω cm^2) is the charge transfer resistance associated with the corrosion redox kinetics, and the value used during corrosion rate calculations, as per [42]; Q (Ω^{-1} cm^{-2} s^n) is a constant phase element that represents the interfacial capacitance of the electrode, n is the exponent associated with Q, R_L (Ω cm^2) is a resistance that is associated with the adsorption process of the intermediate species and L (H cm^{-2}) is a pseudo-inductive contribution of the adsorbed/adsorbing intermediate during the EIS period of the alternating voltage cycle. Concerning corrosion rate calculations, a higher capacitive arc diameter signifies a lower corrosion rate. The effective interfacial capacitance (C_{eff}) was calculated using Q, its exponent n, and the resistance outputs as described in [52], in Eq. (6), i.e.

$$C_{eff}\ (\mu F\ cm^{-2}) = 10^6[(Q^{1/n}\ (R_s^{-1} + R_{ct}^{-1})]^{(n-1)/n} \quad (6)$$

The results of impedance fitting are presented in Table 5, and will be discussed in Section 4 in the context of other results.

3.4.2. Corrosion rate evolution

Fig. 5(a) presents F22 corrosion rates, using R_{ct} values determined from EIS, as a function of immersion time for the three different heat treatment conditions (F22WQ, F22-580 °C/4.5 h and F22-700 °C/3.5 h).

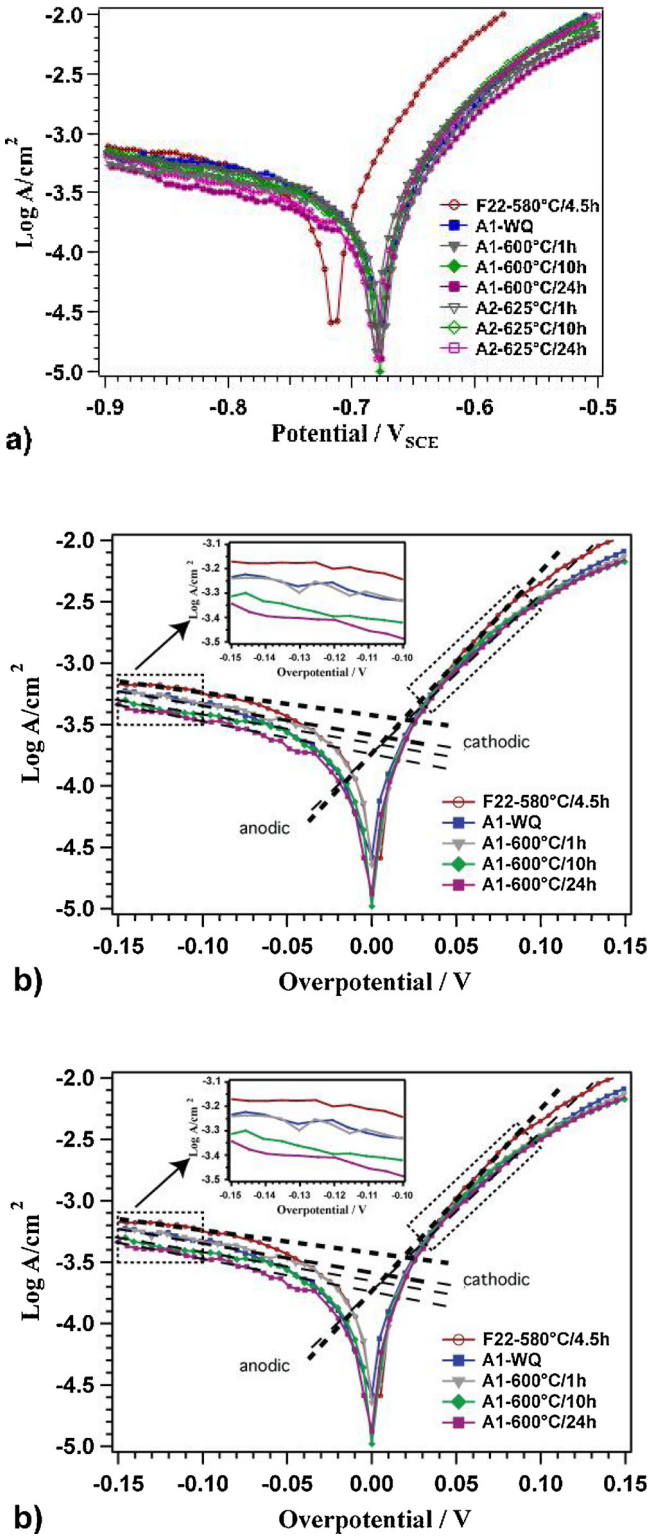

Fig. 3. (a) Log I-E curves of F22-580 °C/4.5 h and all HT10 variants in CO_2-sat. brine electrolyte (T = 60 °C, pH = 5.4, P_{total} = 1 atm, P_{CO2} = 0.8 atm), and (b–c) same data plotted as Log I (A cm^{-2}) vs. overpotential (V).

The quench-hardened sample F22WQ exhibits the highest corrosion rate (˜5.4 (± 0.8) mm/y). Regarding the Q&T F22 steels, i.e. F22-580 °C/4.5 h and F22-700 °C/3.5 h, these reach a corrosion rate of ˜3.8(± 0.3) mm/y and ˜2.9(± 0.2) mm/y respectively after 5 h exposure, which is maintained throughout the remaining immersion period. Note that the increase in tempering temperature from 580 °C to 700 °C results in an alloy (F22-700 °C/3.5 h) with a lower corrosion rate. Fig. 5(b) presents average corrosion rate data for HT10 austenitised at 850 °C for *3.5 h*, Q&T at 600 °C (for 0 h, 1 h, 10 h and 24 h). Similarly, Fig. 5(c) presents corrosion rates for HT10 austenitised at 850 °C for *5.8 h*, Q&T at 625 °C (for 0 h, 1 h, 10 h and 24 h). As observed for F22WQ, the as-quenched HT10 samples also present the highest corrosion rates, which continuously increase throughout the immersion period. With tempering, we always note a relative decrease in corrosion rate with respect to the as-quenched samples. All tempered HT10 samples at both tempering temperatures attain a steady corrosion rate by the 7th hour of immersion. For both tempering temperatures, the HT10 samples tempered for longer corrode with decreasing intensity. Moreover, tempering at higher temperature (625 °C) confers an improved corrosion resistance. It is highlighted that the corrosion rate profiles of tempered HT10 and F22 fall within a similar range, i.e. between 3.0–4.0 mm/y.

Fig. 6 shows the open circuit potential (V_{oc}) values recorded for the F22 and HT10 alloys over 30 h immersion. Relative to F22, the HT10 variants all have a more noble potential. We expect that a slightly higher Cr content combined with that of ˜3% Ni in HT10 is responsible for this higher V_{oc} in HT10 compared to F22, since Ni has a more positive reduction potential with respect to Fe, and serves to ennoble the alloy [56]. Considering only the as-quenched F22 and HT10 alloys, these samples always present the most *positive* open circuit potentials. The V_{oc} for tempered F22 steels were lower, and showed very little variation throughout the tests, apart from the initial 4–5 h. Alloy F22-700 °C/3.5 h experienced the lowest corrosion rates and registered the most negative V_{oc} over the exposure period. The V_{oc} of HT10 alloy variants follow a very similar evolution to each other, i.e. a small initial negative shift is followed by a slow, positive shift at comparable rates. Tempering the alloy, even for 1 h (grey markers), encourages a shift to more negative potential. With longer tempering at both tempering temperatures, more negative (but similar magnitude) open circuit potentials are measured (see purple and green markers in Fig. 6). At the end of the 30 h exposure, the difference in open circuit potential between as-quenched HT10 and 24 h-tempered HT10 is approximately + 20 mV.

3.5. Substrate analysis after 30 h exposure to CO_2-sat. Brine (60 °C)

Fig. 7 presents typical SEM images and EDX spectra of steel surfaces after exposure to CO_2-sat. brine (T = 60 °C, pH = 5.4), with (a) F22-580 °C /4.5 h and (b) HT10 A1-600 °C/10 h chosen as examples. The corroded surfaces appear representative of Cr-containing steels exposed to CO_2-sat. brine as typically reported in the literature [12,22,24,26,27,29,30], where the corrosion product appears cracked and dehydrated after removal from the test electrolyte. As shown in the EDX spectra in Fig. 7(c–d), appreciable signals from the principal lines of Cr, Mo, Fe and O from corroded F22; and of Cr, Mo, Fe, O, V and Ni from corroded HT10 are detected in the corrosion product of each alloy respectively. These are enhanced relative to their counts measured from polished substrates (see Fig. A1 in the Supplementary Materials for comparison). Additional signatures from C and Ca likely result from some, minor precipitation of a calcium-containing compound (e.g. calcium-ferrous carbonate) [33,57]. EDX spectra were also taken from regions (gaps) dividing the cracked corrosion product, and a typical result is shown in Fig. 7(d). The intense signal for Fe from the gap, and the absence of the other signatures from the corresponding EDX spectrum, is comparable to the polished substrate (Fig. A1 in the Supplementary Materials) and appears to come entirely from the steel substrate. Further, to study the possibility of localised corrosion, surface morphologies of samples were examined following the chemical removal of the corrosion product layer using Clarke's solution [38]. Images of these surfaces are presented in Fig. 7(e–f) for F22-580 °C/4.5 h and HT10's A1-600 °C/10 h respectively. We note that after corrosion product removal, a corroded F22 bainitic or HT10 martensitic

Table 4
Extracted potentiodynamic polarisation data for F22 and HT10 steels in CO_2-sat. brine (T = 60 °C, pH = 5.4).

	F22-580 °C/4.5 h	A1-WQ	A1-600 °C/1 h	A1-600 °C/10 h	A1-600 °C/24 h	A2-625 °C/1 h	A1-625 °C/10 h	A2-625 °C/24 h
E_{corr} (mV_{SCE})	−717 (± 4)	−669(± 6)	−674(± 4)	−680(± 2)	−675(± 5)	−680(± 3)	−679 (± 2)	−680(± 2)
I_{corr} (A/cm2)	4.0×10^{-4} (± 3%)	3.2×10^{-4} (± 3%)	3.1×10^{-4} (± 8%)	2.5×10^{-4} (± 5%)	2.0×10^{-4} (± 4%)	3.2×10^{-4} (± 5%)	2.8×10^{-4} (± 2%)	2.4×10^{-4} (± 3%)
CR (mm/y)	4.6	3.7	3.6	2.9	2.3	3.7	3.2	2.8
b_a (mV/dec)	60 (± 3)	68 (± 2)	68(± 2)	67(± 2)	66(± 2)	64(± 3)	62(± 2)	61(± 3)
I_{lim} (-0.125 V) (A/cm2)	6.8×10^{-4} (± 3%)	5.6×10^{-4} (± 3%)	5.5×10^{-4} (± 8%)	4.2×10^{-4} (± 5%)	3.9×10^{-4} (± 4%)	5.9×10^{-4} (± 5%)	5.3×10^{-4} (± 2%)	4.7×10^{-4} (± 3%)
B_{diff}	26 (± 1)	29.5 (± 1)	29.5 (± 1)	29. ± 0.6)	28.5(± 1)	28 (± 1)	27 (± 1)	26.5 (± 1)

microstructure is revealed. These images appear rather comparable with each other and do not reveal any significant localised corrosion morphology (e.g. pits, fissures or other cavities) under the studied conditions after a 30 h exposure period. Indeed, following a systematic evaluation of all acquired SEM images, and reference to a relevant study [21], we conclude that only a characteristic uniform corrosion attack is observed from our specimens for this solution chemistry and time exposure.

4. Discussion

Fig. 8 summarises how austenitising time and tempering temperature/time influence material hardness and average corrosion rate (determined from integrating mean corrosion rate data over the 30 h immersion period). Both material hardness and corrosion rates decrease with higher tempering temperature and/or longer holding time, with the as-quenched states showing highest values for both properties. Corrosion rates of quench & tempered HT10 and F22 are within a comparable range of 3.0–4.0 mm/y. A discussion follows on how tempering softens both materials, and how this might favour CO_2 corrosion resistance.

4.1. As-quenched, and tempered alloy performance: Hardness

The high hardness' (˜360 HV_{30}) of water quench-hardened HT10 and of F22, after austenitisation, are the result of different mechanisms. F22WQ (upper bainite) comprises dislocation-rich bainite plates, packed in sheaves; the elongated precipitates of Fe_3C formed at bainite plate boundaries contribute to hardening (see Fig. 2(a)) [58]. On the other hand, HT10 consists entirely of dislocation-rich martensite after the rapid cooling from austenite (quench treatment). The high hardening results from carbon trapping within the body centred cubic unit cells, giving rise to a tetragonal strain field that has a very strong interaction with dislocation strain fields [58]. Such as-quenched martensitic microstructures comprise abundant point and line lattice defects [58].

The tempering of water quenched F22 decreases its hardness, even after a short heat treatment (e.g. ˜4 h) in the range 580 °C–700 °C, as the stored energy in the quench-hardened microstructure is released. Dislocations are annihilated, any retained austenite is decomposed [58], and carbides (Cementite and M_2C) are precipitated. With the tempering of HT10, as shown in Ref. [35] from synchrotron X-ray diffraction data, carbon diffuses out of the strained body centred cubic unit cells (a phenomenon referred to as a decrease in tetragonality as the c/a ratio of the lattice parameter decreases). During tempering, the carbon in solid solution first reacts with iron to form cementite, followed by reaction with diffusible Mo, V, Cr solute atoms to form small, abundant and matrix-coherent alloy carbides $(Mo, V, Cr)_X$ C precipitates (X = 1 or 2). With tempering, these alloy $(Mo, V, Cr)_X$ carbides nucleate in HT10, and begin to coarsen via Ostwald ripening [59]; simultaneously, the dislocation density begins to decrease [35]. Then, after an optimal period of tempering (for example, 10 h) the alloy would comprise well-dispersed precipitates that are semi-coherent with the matrix in a so-called 'peak-aged' condition. Such a microstructure would offer HT10 a desirable balance of strength and toughness [34]. However, with even longer tempering, one would obtain a lower number density of far coarser carbide precipitates in the material microstructure (over-ageing) [34]. Such carbide dispersion does not contribute significantly to material strength due to a loss of coherency of the carbide precipitates with the matrix; further, with an even lower dislocation density, a softer but tougher alloy is produced [34,35]. Regarding F22, we expect the post-temper softening is also a result of the decrease in dislocation density and the nucleation and growth of carbides (mainly Fe_3C, see Fig. 2(a–b)). For F22-700 °C/3.5 h, the extent of carbide coarsening is greatest with the most significant decrease in dislocation density. It explains why this tempered bainite is the softest material amongst all the studied candidates in the present work.

4.2. As-quenched, and tempered alloy performance: Corrosion

The tempering phenomena discussed in the previous sub-section are expected to modify corrosion kinetics. Before exploring further, we elaborate upon the Cr-enriched surface corrosion product layer observed on F22 and HT10 since this feature was common to all substrates (see Fig. 7 and Fig. A2 in the appendix). Cr is more electrochemically active than the matrix Fe [60], and possesses higher self-passivating capability. After immersion in the corrosive medium, Cr is, thus, expected to dissolve and passivate the base alloy surface through the development of a hydrated chromium oxy(hydroxy) overlayer [56]. We confirm a Cr-enriched overlayer from EDX (Fig. 7(c–d)). By comparing our corroded surfaces with those in the reported literature of low Cr-steel corrosion in CO_2-sat. brines [21–33], where results from characterisation techniques of cross-sectioning, X-ray diffraction, Raman spectroscopy and TEM/EDX are also reported, we suggest that an amorphous $Cr(OH)_3$ has most likely developed on the surfaces of HT10 and F22. The CO_2 corrosion resistance of low-carbon steels is reported to improve with Cr content, evidently due to better film qualities such as improved passivation structure, adherence and reduced permeability to electrolytes [12,23,31]. Alloys with 2–3 wt% Cr, like HT10 and F22, corrode at rates lower than steels containing no Cr, but higher than those containing 4 wt% Cr and above [16,17,21]. Clearly, the wt% of Cr is significant towards improving corrosion resistance.

Further, on reviewing the literature on the CO_2 corrosion performance of different steel microstructures containing the same Cr wt% [6,22,25,31,61], some findings are relevant. Mishra et al. found some improvement to CO_2 corrosion resistance for quenched and tempered 2.25 wt% Cr steels tempered at the highest temperature (samples were tempered at 350 °C, 400 °C and 475 °C for 1 h) [6]. Alves et al suggested that the beneficial effect of Cr towards corrosion resistance in steel must rely on Cr being present as a substitutional solute in the matrix [61], and not 'tied up' as a carbide precipitate [61]. Wu *et al.* compared the CO_2 corrosion resistance (in 3 wt% NaCl at 60 °C and P_{CO2} = 3 bar) of 1 wt% Cr steel in a Q&T martensite, and a ferrite-pearlite form [25]. They report that a tempered martensite microstructure that comprises

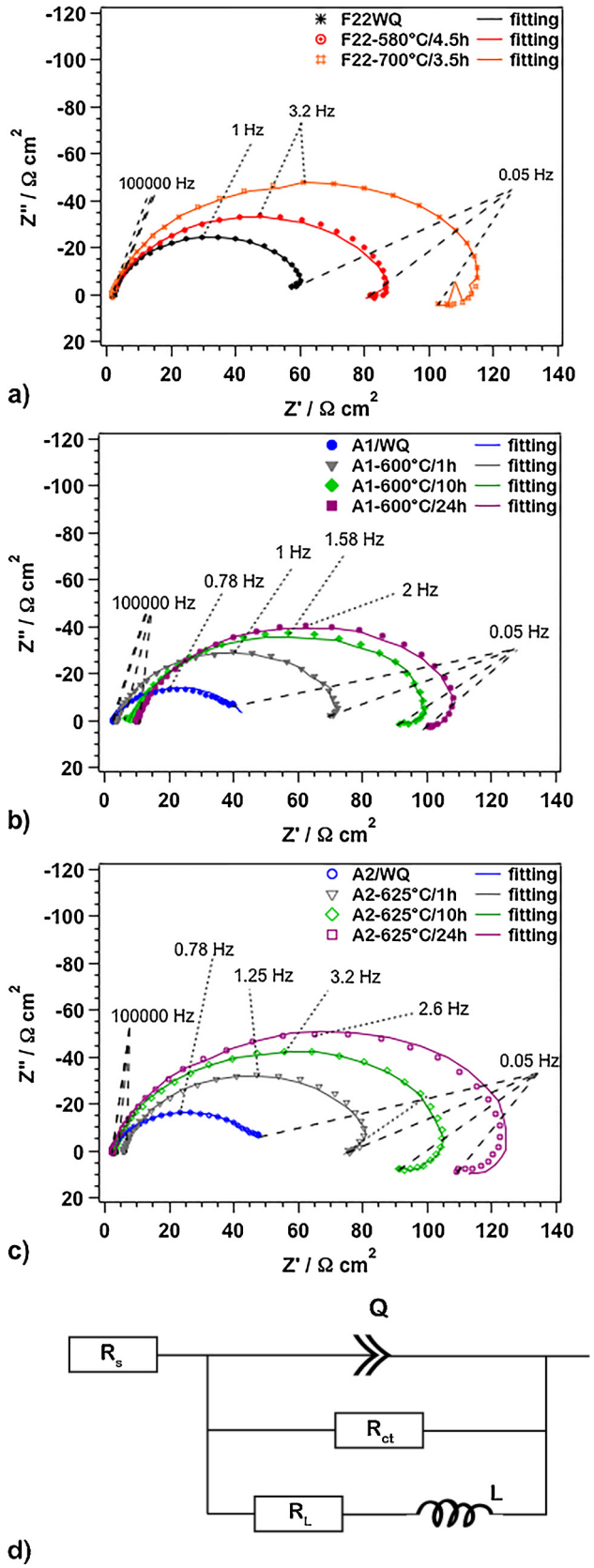

Fig. 4. EIS Nyquist plots and fits of (a) F22 steels and (b–c) HT10 steels, in CO_2-sat. brine electrolyte (T = 60 °C, pH = 5.4, P_{total} = 1 atm, P_{CO2} = 0.8 atm), at the 30th hour of immersion; (d) Equivalent circuit model used to fit all the data.

dispersed Cr-containing carbides would be relatively depleted in Cr if compared against a ferrite-pearlite microstructure with 'free Cr' in solid solution. For the latter case, they inferred that a relatively more protective surface $Cr(OH)_3$ could protect a ferrite-pearlite microstructure. Rather interestingly, such a conclusion was also reported by Li et al. [31], although they compared an as-quenched martensite with the bainitic and ferritic-pearlitic forms of a 3 wt% Cr steel. In their case, however, the as-quenched martensite (which had no precipitated Cr-carbides and all 'free Cr') offered the greatest resistance to corrosion. Their cross-sectional EDX analyses of the metal-electrolyte interface, post-immersion testing, showed that the as-quenched martensite had the highest detectable Cr content. This was inferred to be the primary reason behind greater protection against corrosion.

Referring to the V_{oc} transients (Fig. 6), we consider that the magnitude of a positive shift in open circuit potential could reflect a level of improved protectiveness of an interfacial/surface film [12,62]. Such a profile suggests that a mild passivation effect could be in play and that anodic dissolution is marginally retarded. As Qian et al demonstrate [28], increasing the Cr content (from 0 to 9%) raises the steel's V_{oc} to more positive values. This is largely due to Cr-enrichment of the surface and its retardation of the anodic oxidation reaction of Fe. In our study, by the 30th hour of immersion the as-quenched HT10 and F22 present the highest open circuit potential change (ΔV_{oc}) from their values at immersion, by + 17 mV (± 1 mV). The tempered HT10 variants present ΔV_{oc} of + 10 mV (± 4 mV), whereas tempered F22 steels show a ΔV_{oc}, in the negative direction, of −6 mV (± 2) mV. As a reminder, the matrix Fe (balance), Mo (~1%) and Cr (2.2%) are the primary carbide forming elements in F22 [58]. However, for HT10, it is V (0.45 wt%), Mo (1.5 wt%), and Cr (2.5%) that are the predominant carbide formers [35]. Studies within our research programme have confirmed the depletion of Cr, Mo and V from the matrix during tempering [34,35], as these elements form MC and M_2C alloy carbide compound precipitates. We interpret that this is reflected in the ΔV_{oc} data, where relatively Cr-depleted alloy surfaces might not produce as strong a positive shift (i.e. passivation effect) over the 30 h immersion period if compared to a surface where the carbide-forming alloying elements are 'free' in the solid solution. Thus, like Li et al. [31], we hypothesise that the level of Cr-enrichment is greatest in the *as-quenched* HT10 and *as-quenched* F22 alloy corrosion product layers, since Cr and Mo are present as substitutional solutes in the matrix. Indeed, one amongst the many suggested roles of alloyed Mo towards its beneficial corrosion resistance relates to encouraging Cr-enrichment of the surface film [63,64]. With longer tempering, on the other hand, both Cr and Mo are 'lost' to carbide formation; the relative V_{oc} response becomes more negative.

Importantly, however, the magnitude of ΔV_{oc} is always quite small, and the polarisation and EIS data (Figs. 3 and 4) indicate that as-quenched alloys suffer the worst corrosion rates, i.e. the i_{corr} values are highest. Related measurements that are worth discussing further are the interfacial capacitance data presented in Table 5. The C_{eff} (μF cm^{-2}) is indicative of the space-charge distribution at the surface and can be informative about the state of the metal/electrolyte interface. While the values for interfacial capacitance of tempered F22 are more representative of corroding iron surfaces (i.e. 50–200 μF cm^{-2}) [65], those of HT10 and as-quenched F22 are peculiarly high. The as-quenched alloys, in particular, exhibit abnormally high capacitances (between 1000–3000 μF cm^{-2}) after 30 h corrosion. With tempering, however, decreasing capacitances are recorded. Our estimates decrease from 1150 μF cm^{-2} to 230 μF cm^{-2} as a function of tempering time. We interpret that the high capacitance measurements of as-quenched samples is the result of severe corrosion (Fig. 5), serving to roughen the interface and increase the effective electroactive area. With tempering, the measured decrease in corrosion rates should correlate with lower surface roughening, and a relative drop in interfacial capacitance. Even though similar corrosion rates, between 3–4 mm/y are measured for HT10 and F22, the former alloy, a Ni-Cr-Mo martensite steel, still exhibits far higher capacitance. With reference to the V_{oc} data (Fig. 6) and

Table 5
Extracted electrochemical equivalent circuit modelling parameters of EIS data measured from F22 and HT10 steels immersed in CO_2-sat. brine (T = 60 °C, pH = 5.4, t = 30 h).

	R_s ($\Omega\,cm^2$)	R_{ct} ($\Omega\,cm^2$)	Q ($\Omega^{-1}\,cm^2\,s^n$)	n	C_{eff} ($\mu F\,cm^{-2}$)	R_L ($\Omega\,cm^2$)	L ($H\,cm^{-2}$)
F22WQ	2.1	63.8	3283.8	0.85	1310.2	597.4	648.9
A1-WQ	3.1	39.2	8367.4	0.75	2370.8	–	–
A2-WQ	2.2	47.5	6137.0	0.77	1683.3	–	–
F22-580 °C/4.5 h	1.4	91.9	1025.2	0.78	156.1	432.2	667.1
F22-700 °C/3.5 h	2.1	110.8	757.2	0.79	142.3	744.6	463.8
A1-600 °C/1 h	3.8	74.4	2964.3	0.83	1157.1	663.0	462.9
A2-625 °C/1 h	6.0	82.0	2110.3	0.85	988.6	457.3	284.0
A1-600 °C/10 h	8.2	99.5	1546.5	0.82	595.2	519.0	360.0
A2-625 °C/10 h	2.7	109.3	763.1	0.84	241.6	373.9	274.9
A1-600 °C/24 h	8.8	105.0	1246.0	0.80	409.5	494.4	287.6
A2-625 °C/24 h	2.3	134.7	743.9	0.85	231.1	502.1	487.7
χ2 error	*< 0.01*	*< 0.01*	*0.015*	*< 0.01*	–	*< 0.03*	*< 0.06*

the EDX (Fig. 7), we speculate, further, that the different dielectric properties of the interfacial corrosion product film on HT10 (for instance, the higher base Cr-content, the incorporation of substitutional nickel, the possible presence of vanadium and molybdenum oxides, and the abundant alloy carbides subsequent to tempering) might contribute to its comparatively higher interfacial capacitance. Finally, no clear trend is apparent from the EIS fitted parameters of R_L and L, as a function of tempering. It may imply that the magnitude of the surface relaxation/adsorption responses are similar amongst the studied alloy candidates and are not too influential with respect to modifying corrosion intensity.

Referring again to the V_{oc} data (Fig. 6), the as-quenched HT10 (blue markers) and F22 (black markers) always exhibit the most noble open circuit potentials, which become more negative with tempering for longer time and/or tempering at higher temperature. Using the principles of mixed potential theory (Evans diagrams) [66], a more negative V_{oc} transient that is associated with lower corrosion rates (Fig. 5), signifies low or decreasing cathodic reaction kinetics. Indeed, HT10 polarisation curves in Fig. 3, where diffusion-controlled cathodic corrosion kinetics decrease with tempering, might allow this interpretation to be extended here. Thus, having observed corrosion rates of tempered alloys in a similar range, we propose that the Cr-enriched films formed on HT10 and F22 over 30 h corrosion in CO_2-sat. simulated oilfield brine in this study must be semi-protective at best and offer comparable anti-corrosion properties to each other (within a small range). At least, from the techniques used in the present study, it is difficult to isolate and distinguish their protective qualities. For instance, Fig. A2 in the Supplementary Materials shows how morphologies of the Cr-enriched corrosion product bearing surfaces of as-quenched/tempered HT10 appear indistinguishable. On the basis of the above discussion, we consider that the important corrosion resistive properties of HT10 and F22 are not predominantly related to the Cr-rich surface-filming, but rather determined by modifications that are inherent to the bulk metallurgy brought about by tempering.

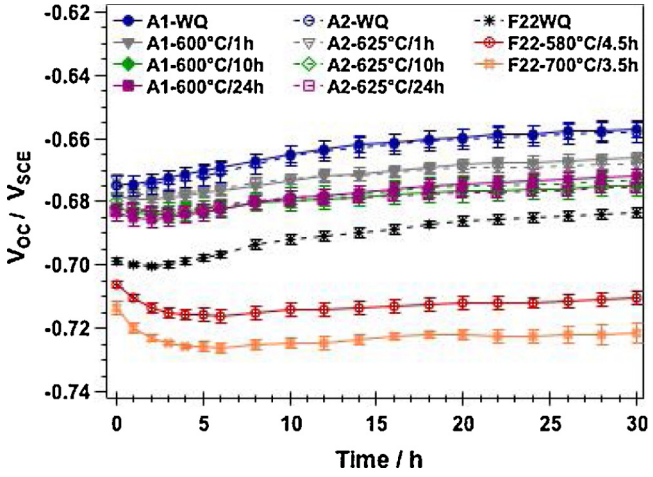

Fig. 6. Evolution of open circuit potential (V_{oc}) for F22 and HT10 steels immersed CO_2-sat. brine (T = 60 °C, pH = 5.4, P_{total} = 1 atm, P_{CO2} = 0.8 atm). Error bars are standard deviations determined from 3 datasets each.

Looking at the corrosion rate - immersion time data in Fig. 5, we hypothesise that the higher structural heterogeneity within as-quenched microstructures causes them to be more reactive than the tempered variants [67]. The as-quenched alloys are rich in point and line crystalline lattice defects, particularly dislocations. Metal atoms adjacent to a dislocation core intersecting the exposed metal surface have higher free energy than atoms distant from it, which could suggest that emergent ends of edge/screw dislocations represent sites for preferential corrosion redox reactions [68–70]. A greater abundance of these would encourage iron dissolution, via direct oxidation or driven by reduction. In addition, some retained austenite in the as-quenched microstructures may contribute to corrosion in HT10 and F22 via

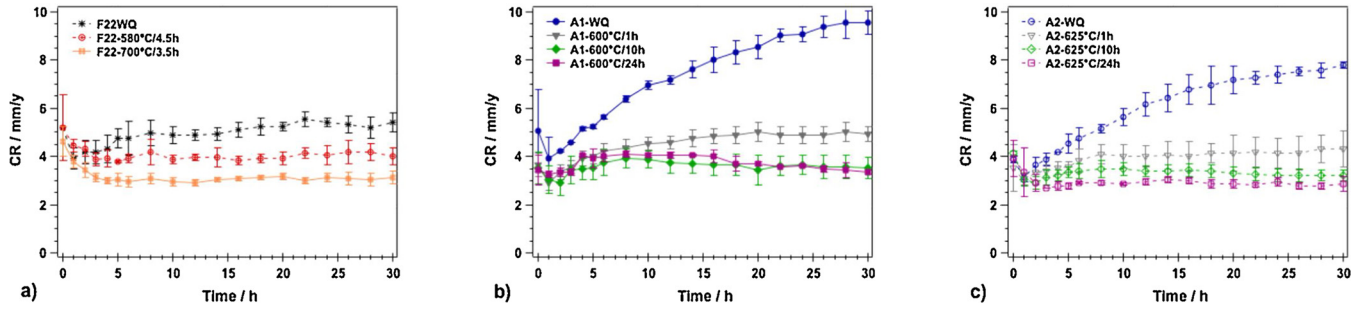

Fig. 5. Corrosion rates (CR) in mm/y as a function of immersion time (h) for different heat treatment conditions of (a) F22 and (b–c) HT10 steels in CO_2-sat. brine electrolyte (T = 60 °C, pH = 5.4, P_{total} = 1 atm, P_{CO2} = 0.8 atm). Error bars are standard deviations determined from at least 3 datasets each.

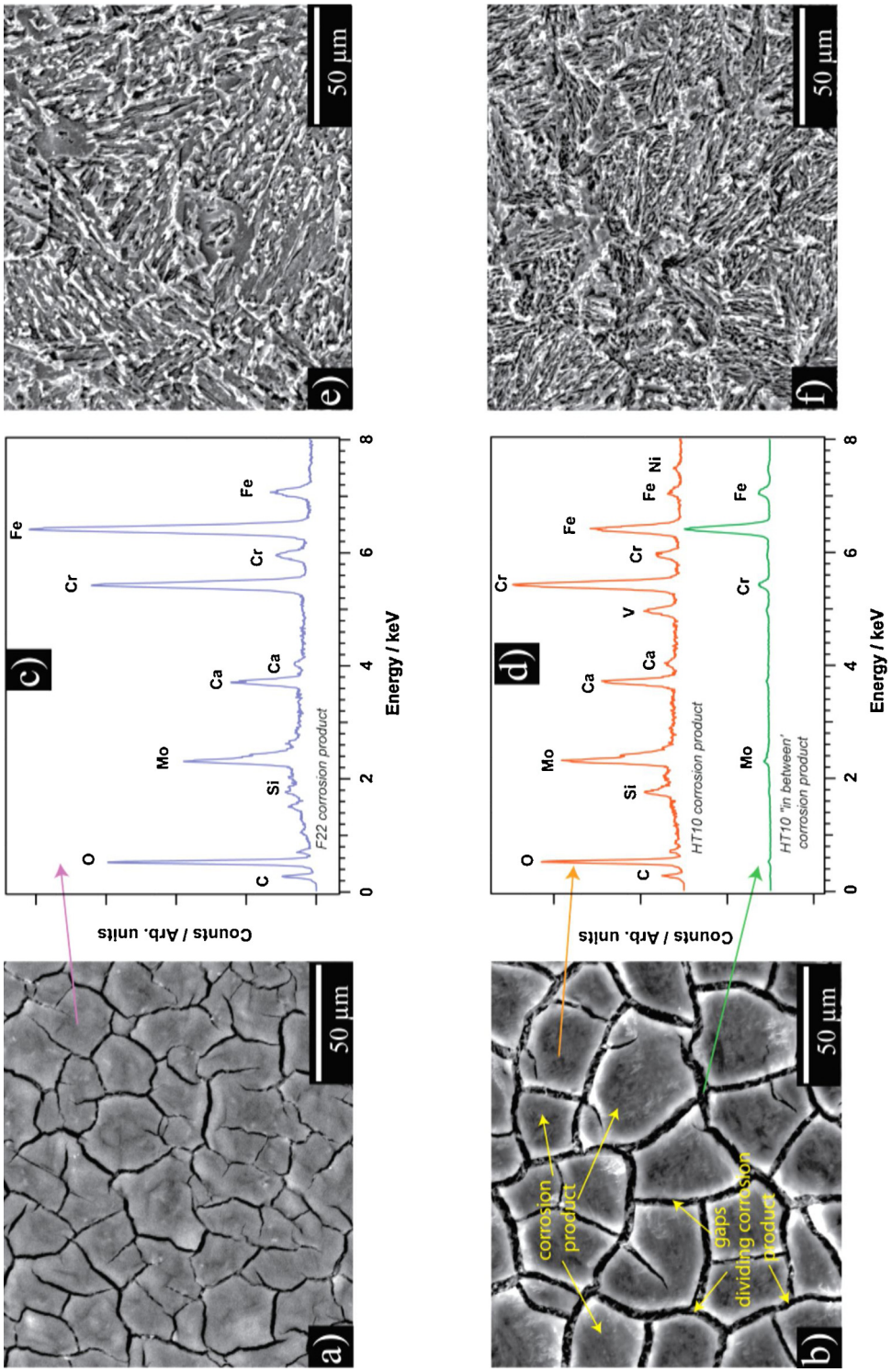

Fig. 7. SEM image (a–b) and EDX spectrum (c–d) from post-corrosion surface of F22-700 °C/3.5 h and HT10 (A1-600 °C/10 h) respectively; SEM image (e–f) of F22-700 °C/3.5 h and HT10 (A1-600 °C/10 h) respectively, after corrosion product removal treatment with Clarke's solution.

microscopic galvanic contributions at ferrite-austenite interfaces, therein promoting ferrite dissolution [71]. The higher, sustained corrosion of quench-hardened HT10 would be a mechanism by which the material relieves stored energy through the metal/electrolyte interface.

In contrast, as a function of tempering temperature and time, (i) the lattice strain relief through a loss of tetragonality, (ii) the coarsening alloy carbide distribution, and (iii) the decreasing dislocation density must play the main role towards lowering CO_2 corrosion rates of tempered HT10 and F22. On reviewing the potentiodynamic polarisation curves in Fig. 3(b–c), the overlapping anodic gradients imply that the anodic dissolution mechanism is not affected by the tempering-induced changes. The cathodic reaction curves overlap near E_{corr}, before being limited by diffusion control at higher overpotential. A decrease of the HT10 cathodic curves is noted that correlates quite well with an increase in tempering time. Assessing $I_{lim,\ c}$ at -0.125 V, this value changes in the temper holding time order: 24 h < 10 h < 1 h < 0 h at both tempering temperatures of 600 °C and 625 °C (see Table 4). To explore the reasons behind these changes, we consider metallurgical changes to

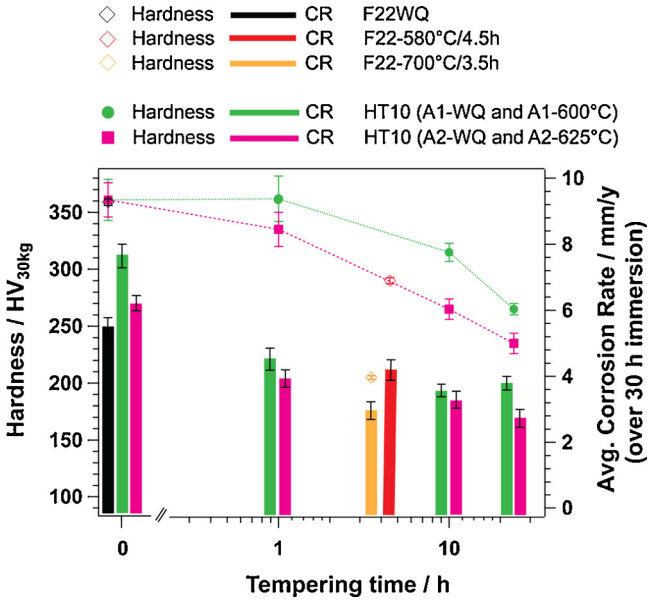

Fig. 8. Summary plot showing F22 and HT10 material hardness and mean EIS Corrosion rate over 30 h immersion in CO_2-sat. brine electrolyte (T = 60 °C, pH = 5.4, P_{total} = 1 atm, P_{CO2} = 0.8 atm), both as a function of tempering time after water quench hardening.

HT10 in further detail.

Fig. 9 presents HT10 metallurgy data taken from Ref [35] for a tempering treatment at 600 °C over 24 h. The average CO_2 corrosion rates, from our study, are included for comparison. More specifically, Fig. 9 plots changes to dislocation density from synchrotron X-ray diffraction (SXRD), Fig. 9(a)); and Matcalc modelled alloy carbide precipitate evolution, Fig. 9(b). Both are presented as a function of holding time at a tempering temperature of 600 °C (see Ref. [35] for more details on the methodology of measurement/calculation). Focusing on Fig. 9(a), the changes to the dislocation structure recovery generally correlate with an average decrease in CO_2 corrosion rates, as a function of tempering time. Results from SXRD indicate that dislocation density decreases by one order of magnitude, from ~2×10^{15} m^{-2} (0 h) to ~1.5×10^{14} m^{-2} (at 24 h) over the entire tempering period [35]. Although not determined explicitly, the dislocation density is expected to be even lower if tempered at higher temperature (625 °C), and may well contribute to the improved corrosion resistance. Longer tempering times at the highest temperatures would annihilate a greater dislocation density, previously inherited from quenching. We anticipate that such recovery would lower the net surface redox reactivity of HT10, as high corrosion rates are possibly obtained at sites where high concentrations of dislocations intersect the exposed electroactive surface [70]. With the support of polarisation data in Fig. 3, we propose that a decrease in dislocation density contributes to decreasing the net cathodic current density supported at the HT10/CO_2-sat. brine electrolyte interface.

Fig. 9(b) presents data outputs from MatCalc modelling work on alloy carbide evolution in water-quenched HT10 as a function of holding time at tempering temperature of 600 °C, reproduced from Ref. [35]. The bar graphs depict the quantity (phase fraction (unitless) × number density (number/m^3), while the symbols represent the mean size, of the key alloy carbide precipitates ($_{\alpha}$MC, $_{\gamma}$MC and $_{\alpha}M_2C$). Both types of α-type alloy carbides increase in size with tempering. This increase is quite pronounced beyond 10 h of tempering, corresponding to a loss of their coherency with the matrix [35]. On assessing the quantity of all alloy carbides, the number of precipitates remains consistent over 10 h, before decreasing by the 24th hour of tempering. In other words, the longer tempering of HT10 produces a precipitate dispersion comprising a lower number density of larger alloy carbides.

Conceivably, the total cathodic current response at the steel

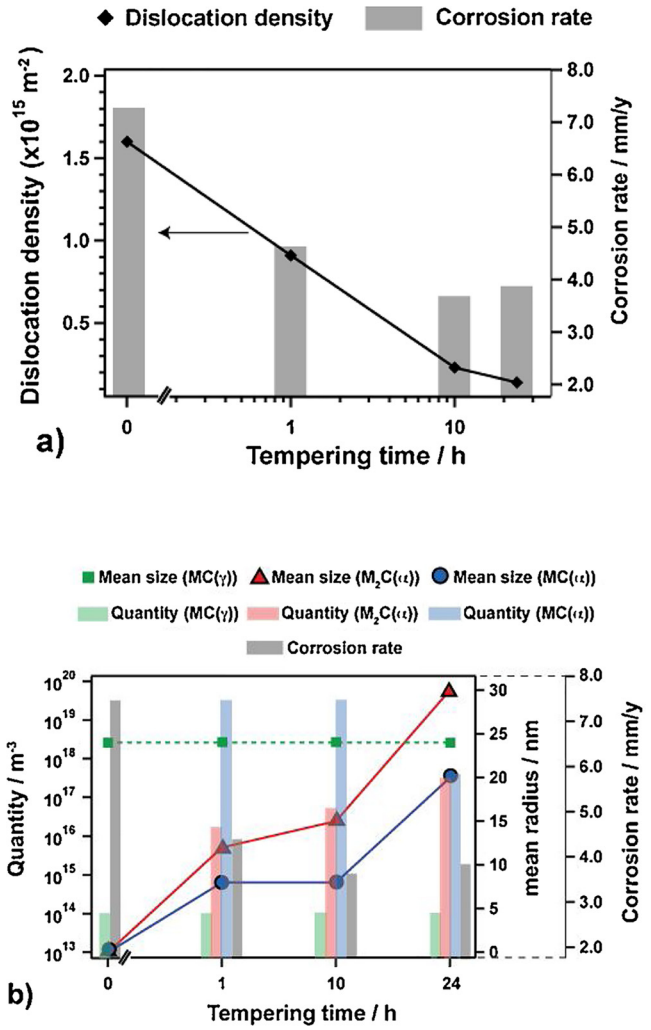

Fig. 9. (a) Changes in dislocation density as a function of tempering time at 600 °C, as measured using Synchrotron X-ray diffraction; (b) Alloy carbide precipitate evolution at 600 °C using Matcalc modelling, where quantity is determined as the product of alloy carbide phase fraction and number density (m^{-3}). Mean EIS Corrosion rates (right y-axis) over 30 h immersion in CO_2-sat. brine electrolyte (T = 60 °C, pH = 5.4, P_{total} = 1 atm, P_{CO2} = 0.8 atm) are included for comparison. The data in this figure are published in Ref. [35], and reproduced here with the permission of the authors.

electrode/aqueous electrolyte interface is supported at many participating substrate-electrolyte interfaces hosting the reduction electrochemistry, such as dislocation core/electrolyte, deformed metal/electrolyte; metal oxide/electrolyte; and alloy carbide/electrolyte (e.g. $(Mo,V,Cr)_XC$) interfaces. Focusing on the abundant transition metal carbides, i.e. MC and M_2C types within the HT10 microstructure, where M = V,Mo,Cr, we highlight that these are widely acknowledged as efficient catalysts for the hydrogen evolution reaction in hydrolysis applications for hydrogen evolution [72,73]. For instance, Fe-doped Mo_2C nanomaterials exhibit high stability and catalytic activity towards cathodic hydrogen evolution compared against isolated Mo_2C [74]. We propose here that the distribution of such d-d-block transition metal carbides embedded in the Fe-matrix in HT10 must, via galvanic action, contribute to the cathodic reaction electrochemistry [72,73], therein causing Fe dissolution [10]. If the net interfacial contact area between the carbides and the matrix were high, e.g. after 1 h temper when dispersed alloy carbides are smallest, coherent and most abundant [35], the supported cathodic current density and, therefore, the net corrosion rate should be higher. Indeed, the electrochemical data of HT10 A1-600 °C/1 h in Figs. 3(b–c) and 5(b–c) show this to be the case. We note

that this must necessarily include the effect of the high dislocation density, as discussed earlier.

All steel working-electrodes in the electrochemical corrosion investigations were immersed and studied in the same CO_2-sat. electrolyte chemistry with the same mode of mass-transfer (static, no stirring). Thus, neither the concentration/diffusion coefficient of the electroactive species nor the interfacial diffusion layer thicknesses, drastically change across the individual experiments. This has offered a good reproducibility of observation. Despite accounting for the geometric surface area in all corrosion current calculations, we have observed differences in the current-carrying capacity of the various heat-treated HT10 alloy samples in the cathodic reaction domains in the polarisation curves (Fig. 3). With tempering, the alloy carbides coarsen and decrease in number density, resulting in a lower net interfacial area to bulk particle volume ratio. By remembering that the dislocation density also decreases with tempering, it is possible to speculate that the number of potential cathodic reaction sites (effective surface area) for a normalised surface area will also decrease. If this were to occur, the contribution to the total cathodic current density should also drop. In turn, lower cathodic reaction kinetics would decrease the general corrosion rate. Thus, with reference to Eq. (5), as n, F, D, C_b and δ are not changed, we conclude it is the effective or true electroactive surface area (cm^{-2}) on the geometrically-normalised alloy surfaces that must support the limiting cathodic current to varying extent as a function of tempering. Fig. 10 presents a schematic of the discussed microstructural changes, on the nanoscale, and their effect on measured material corrosion rates (dashed line).

To support this hypothesis further, the corrosion rate differences between HT10 A1-WQ and HT10 A2-WQ over 30 h in CO_2-sat. brine (Fig. 5(b–c)) are evaluated. As indicated earlier, and in Refs. [34,35], a dispersion of larger spherical $_{\gamma}$MC precipitates remains in the as-quenched HT10 microstructure after austenitisation at 850 °C. While the prior austenite grain size and dislocation densities in the two as-quenched HT10 conditions are similar, A2-WQ comprises a lower number density of larger spherical $_{\gamma}$MC precipitates compared to A1-WQ. From the hypothesis that these precipitates are cathodically electroactive sites, the corrosion kinetics in A2-WQ (lower effective surface area contribution of the $_{\gamma}$MC precipitates) would be slightly lower due to a lower net galvanic interaction between matrix Fe and the $_{\gamma}$MC precipitates. As this is found to be the case over the 30 h immersion, it would suggest that such a lower number density dispersion of large spherical $_{\gamma}$MC marginally improves corrosion resistance. We thus extend such logic to the changing dispersion of the finer $_{\alpha}$MC and $_{\alpha}M_2C$ precipitates that result from the tempering heat-treatment of HT10. In conclusion, tempering at higher temperature has the most significant effect on the metallurgical processes of coarsening carbides and decreasing dislocation density, and therefore favours lower net interfacial redox activity (lower uniform corrosion).

5. Conclusions

The corrosion resistances of a variety of austenitised, quench and temper heat treatments of a newly developed, secondary-hardening martensitic steel (HT10) and a commercial grade steel (ASTM A182 F22) were determined in a CO_2-sat. brine (T = 60 °C, pH = 5.4, P_{total} = 1 atm, P_{CO2} = 0.8 atm) using electrochemical methods. Tempered HT10 and F22 were measured to corrode at comparable rates, in the range of 3–4 mm/y. The modification of austenitising time, tempering temperature and holding time results in a change in precipitated alloy carbide number density and size, as well as dislocation density, which in turn changes the material hardness and corrosion rate. While as-quenched HT10 and F22 present the highest uniform corrosion rates, largely due to the high lattice strains/dislocation densities developed after rapid cooling from austenite, the tempering treatment brings about an improvement in corrosion resistance and a decrease in hardness. Allowing for a comparable role played by a Cr-enriched semi-protective corrosion product overlayer in both alloys, we conclude that the improvement in corrosion resistance with tempering is largely a function of (i) the annihilation of dislocation density, and (ii) the coarsening of the alloy carbide precipitates (associated with a relief in lattice strains and a lower net contribution to the cathodic reaction current density). Noting the correlation between hardness and corrosion rate measurements, the metallurgical tempering phenomena kinetics are deemed to be greater at the higher tempering temperatures. The combination of high temperature tempering and long holding time would thus produce a softer but tougher alloy with improved resistance against uniform CO_2 corrosion under the explored experimental conditions.

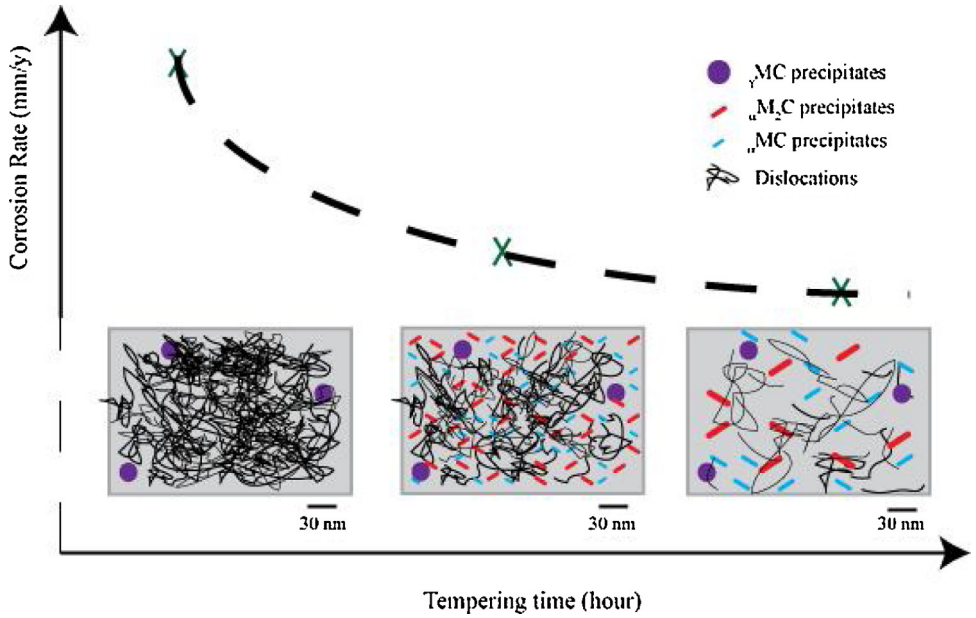

Fig. 10. Schematic of microstructural changes (dislocation density/carbide evolution) and measured uniform corrosion rates as a function of tempering time for Ni-Cr-Mo-V martensitic HT10 steel.

Funding

The work received funding from BP through the BP International Centre for Advanced Materials (BP-ICAM) [BP-ICAM 02].

Data availability

The raw and processed data required to reproduce these findings are available to download from Mendeley data - http://doi:10.17632/j4vfxfnt9j.1 [75].

Acknowledgments

The authors would like to acknowledge the funding and technical support from BP through the BP International Centre for Advanced Materials (BP-ICAM), which made this research possible.

Appendix A. Supplementary data

Supplementary material related to this article can be found, in the online version, at doi:https://doi.org/10.1016/j.corsci.2019.03.036.

References

[1] A. Belani, S. Orr, A systematic approach to hostile environments, J. Pet. Technol. 60 (2008) 34–39.
[2] L.T. Popoola, A.S. Grema, G.K. Latinwo, B. Gutti, A.S. Balogun, Corrosion problems during oil and gas production and its mitigation, Int. J. Ind. Chem. 4 (2013) 1–15, https://doi.org/10.1186/2228-5547-4-35.
[3] H.K.D.H. Bhadeshia, Prevention of hydrogen embrittlement in steels, ISIJ Int. 56 (2016) 24–36.
[4] M.B. Kermani, A. Morshed, carbon dioxide corrosion in oil and gas production—a compendium, Corrosion 59 (2003) 659.
[5] L.S. Moiseeva, Carbon dioxide corrosion of oil and gas field equipment, Prot. Met. 41 (2005) 76–83.
[6] B. Mishra, D.L. Olson, M.M. Salama, S. Al-Hassan, Effect of microstructure on corrosion of steels in aqueous solutions containing carbon dioxide, Corrosion 54 (1998) 480–491.
[7] A. Dugstad, H. Hemmer, M. Seiersten, Effect of steel microstructure on corrosion rate and protective Iron carbonate film formation, Corrosion. 57 (2001) 369–378.
[8] D. Clover, B. Kinsella, B. Pejcic, R. De Marco, The influence of microstructure on the corrosion rate of various carbon steels, J. Appl. Electrochem. 35 (2005) 139–149.
[9] D. Lopez, T. Perez, S. Simison, The influence of microstructure and chemical composition of carbon and low alloy steels in CO_2 corrosion. A state-of-the-art appraisal, Mater. Des. 24 (2003) 561–575.
[10] J.L. Mora-mendoza, S. Turgoose, Fe_3C influence on the corrosion rate of mild steel in aqueous CO 2 systems under turbulent flow conditions, Corros. Sci. 44 (2002) 1223–1246.
[11] C.I. Ossai, Advances in asset management techniques: an overview of corrosion mechanisms and mitigation strategies for oil and gas pipelines, ISRN Corros. 2012 (2012) 1–10.
[12] S. Hassani, T.N. Vu, N.R. Rosli, S.N. Esmaeely, Y. Choi, D. Young, et al., Wellbore integrity and corrosion of low alloy and stainless steels in high pressure CO_2 geologic storage environments: an experimental study, Int. J. Greenh. Gas Control. 23 (2014) 30–43.
[13] R. De Marco, W. Durnie, A. Jefferson, B. Kinsella, A. Crawford, Persistence of carbon dioxide corrosion inhibitors, Corrosion 58 (2002) 354–363.
[14] S. Turgoose, G.E. Dicken, J.W. Palmer, Review of issues associated with inhibition of scale-deposit-covered pipelines, SPE Int. Oilf. Corros. Symp. (2006) p. SPE 100728.
[15] K. Denpo, H. Ogawa, Effects of nickel and chromium on corrosion rate of linepipe steel, Corros. Sci. 35 (1993) 285–288.
[16] P.I. Nice, H. Takabe, M. Ueda, The Development and Implementation of a New Alloyed Steel for Oil and Gas Production Wells, NACE International, 2000 Paper No. 154.
[17] M.B. Kermani, J.C. Gonzales, C. Linne, M. Dougan, R. Cochrane, Development of Low Carbon Cr-Mo Steels With Exceptional Corrosion Resistance for Oilfield Applications, NACE International, 2001 Paper No. 01065.
[18] D.S. Carvalho, C.J.B. Joia, O.R. Mattos, Corrosion rate of iron and iron-chromium alloys in CO2 medium, Corros. Sci. 47 (2005) 2974–2986.
[19] L.N. Xu, S.Q. Guo, C.L. Gao, W. Chang, T.H. Chen, M.X. Lu, Influence of microstructure on mechanical properties and corrosion behavior of 3%Cr steel in CO_2 environment, Mater. Corros. 63 (11) (2012).
[20] W. Zhang, L. Xu, S. Guo, S. Zhang, M. Lu, Y. Zang, Corrosion behaviour of novel Cr2MoNbTi pipeline steel in CO_2 environment, Int. Pipeline Conf. (2012) code IPC2012-90692.
[21] C.F. Chen, M.X. Lu, D.B. Sun, Z.H. Zhang, W. Chang, Effect of chromium on the pitting resistance of oil tube steel in a carbon dioxide corrosion system, Corrosion 61 (2005) 594–601.
[22] T. Chen, L. Xu, M. Lu, W. Chang, L. Zhang, Study of Factors Affecting Low Cr Alloy Steels in a CO_2 Corrosion System, iNACE International, 2011 Paper No. 11074.
[23] S. Guo, L. Xu, L. Zhang, W. Chang, W. Minxu, Corrosion of alloy steels containing 2% chromium in CO2 environments, Corros. Sci. 63 (2012).
[24] Y. Xie, L. Xu, C. Gao, W. Chang, M. Lu, Corrosion behavior of novel 3%Cr pipeline steel in CO_2 Top-of-Line Corrosion environment, Mater. Des. 36 (2012) 54–57.
[25] Q. Wu, Z. Zhang, X. Dong, J. Yang, Corrosion behavior of low-alloy steel containing 1% chromium in CO_2 environments, Corros. Sci. 75 (2013) 400–408.
[26] L. Xu, S. Guo, W. Chang, T. Chen, L. Hu, M. Lu, Corrosion of Cr bearing low alloy pipeline steel in CO_2 environment at static and flowing conditions, Appl. Surf. Sci. 270 (2013) 395–404.
[27] Z. Liu, X. Gao, L. Du, J. Li, Y. Kuang, B. Wu, Corrosion behavior of low-alloy steel with martensite / ferrite microstructure at vapor-saturated CO_2 and CO_2-saturated brine conditions, Appl. Surf. Sci. 351 (2015) 610–623.
[28] Y.H. Qian, D. Niu, J.J. Xu, M.S. Li, The influence of chromium content on the electrochemical behavior of weathering steels, Corros. Sci. 71 (2013) 72–77.
[29] J. Zhu, L. Xu, M. Lu, L. Zhang, W. Chang, L. Hu, Essential criterion for evaluating the corrosion resistance of 3Cr steel in CO_2 environments: Prepassivation, Corros. Sci. 93 (2015) 336–340.
[30] S. Guo, L. Xu, L. Zhang, W. Chang, M. Lu, Characterization of corrosion scale formed on 3Cr steel in CO_2-saturated formation water, Corros. Sci. 110 (2016) 123–133.
[31] W. Li, L. Xu, L. Qiao, J. Li, Effect of free Cr content on corrosion behaviour of 3Cr steels in a CO_2 environment, Appl. Surf. Sci. 425 (2017) 32–45.
[32] Y. Choi, S. Nešic, H. Jung, Effect of alloying elements on the corrosion behavior of carbon steel in CO2 environments, Corrosion 74 (2018) 566–576.
[33] B. Wang, L. Xu, G. Liu, M. Lu, Corrosion behavior and mechanism of 3Cr steel in CO_2 environment with various Ca^{2+} concentration, Corros. Sci. 136 (2018) 210–220.
[34] T.I. Ramjaun, S.W. Ooi, R. Morana, H.K.D.H. Bhadeshia, Designing steel to resist hydrogen embrittlement Part 1 – trapping capacity, Mater. Sci. Technol. (2018) 1–23.
[35] S.W. Ooi, T.I. Ramjaun, R. Morana, M. Drakopoulos, H.K.D.H. Bhadeshia, Designing steel to resist hydrogen embrittlement Part 2 – precipitate characterisation, Mater. Sci. Technol. (2018) 1–32.
[36] S. Yamasaki, Modelling Precipitation of Carbides in Martensitic Steels, Cambridge, (2004).
[37] G.R. Joshi, K. Cooper, X. Zhong, T. Cook, E. Ahmad, N. Harrison, et al., Temporal evolution of sweet oilfield corrosion scale: phases, morphologies, habits, and protection, Corros. Sci. 142 (2018) 110–118.
[38] A.S.T.M. Standard, G1-03: “Standard Practice for Preparing, Cleaning and Evaluating Corrosion Test Specimens,”, (2019).
[39] J. Tafel, Uber die Polarisation bei kathodischer Wasserstoffentwicklung, Z. für Phys. Chemie/international J. Res. Phys. Chem. Chem. Phys. (1905) 641.
[40] C. Wagner, W. Traud, On the interpretation of corrosion processes through the superposition of electrochemical partial processes and on the potential of mixed electrodes, Elektrochem. 44 (1938) 391.
[41] M. Stern, A.L. Geary, Electrochemical polarization: I. A theoretical analysis of the shape of polarization curves, J. Electrochem. Soc. 104 (1957) 56.
[42] J.R. Scully, Polarization resistance method for determination of instantaneous corrosion rates, Corrosion 56 (2000) 199–218.
[43] Z. Zeng, R.S. Lillard, H. Cong, Effect of salt concentration on the corrosion behavior of carbon steel in CO_2 environment, Corrosion 72 (2016) 805–823.
[44] J.H. Holloman, L.D. Jaffe, Time-tempering relations in tempering steel, Metall. Trans. (1945) 223–249.
[45] S. Murphy, J.H. Woodhead, An investigation of the validity of certain tempering parameters, Metall. Trans. (1972) 727–735.
[46] L.G. Gray, B.G. Anderson, M.J. Danysh, P.R. Tremaine, Effect of pH and Temperature on the Mechanism of Carbon Steel Corrosion by Aqueous Carbon Dioxide, NACE International, 1990 paper No. 040.
[47] S. Nesic, J.L. Crolet, D.M. Drazic, Electrochemical Properties of Iron Dissolution in the Presence of Carbon Dioxide - Basics Revisted, NACE International, 1996 Paper No. 003.
[48] A. Kahyarian, B. Brown, S. Nesic, Electrochemistry of CO_2 corrosion of mild steel: effect of CO2on iron dissolution reaction, Corros. Sci. 129 (2017) 146–151.
[49] E. Remita, B. Tribollet, E. Sutter, V. Vivier, F. Ropital, J. Kittel, Hydrogen evolution in aqueous solutions containing dissolved CO_2: quantitative contribution of the buffering effect, Corros. Sci. 50 (2008) 1433–1440.
[50] E. Protopopoff, P. Marcus, Corrosion Mechanisms in Theory and Practice, 2nd ed., Marcel Dekker, New York, 2002.
[51] Y. Lu, H. Jing, Y. Han, L. Xu, Effect of temperature on the 3Cr low-alloyed steel initial corrosion behavior in CO_2 solution, Mater. Chem. Phys. 178 (2016) 160–172.
[52] B. Hirschorn, M.E. Orazem, B. Tribollet, V. Vivier, I. Frateur, M. Musiani, Determination of effective capacitance and film thickness from constant-phase-element parameters, Electrochim. Acta 55 (2010) 6218–6227.
[53] M. Keddam, O.R. Mattos, H. Takenouti, Mechanism of anodic dissolution of iron-chromium alloys investigated by electrode impedances - I. Experimental results and reaction model, Electrochim. Acta 31 (1986) 1147–1158.
[54] D.C. Silverman, Corrosion rate estimation from pseudo-inductive electrochemical impedance response, Corrosion 45 (1989) 824–830.
[55] T. das Chagas Almeida, M.C.E. Bandeira, R.M. Moreira, O.R. Mattos, New insights on the role of CO_2 in the mechanism of carbon steel corrosion, Corros. Sci. 120 (2017) 239–250.
[56] K. Hashimoto, K. Asami, M. Naka, T. Masumoto, The role of alloying elements in improving the corrosion resistance of amorphous iron base alloys, Corros. Sci. 19

(1979) 857–867.
[57] S.N. Esmaeely, Y. Choi, D. Young, S. Nešic, Effect of Calcium on the Formation and Protectiveness of Iron Carbonate Layer in CO_2 Corrosion, Corrosion 69 (2013) 912–920.
[58] H.K.D.H. Bhadeshia, R.W.K. Honeycombe, Steels: Microstructure and Properties, 3rd ed., Butterworths-Heinemann, 2006.
[59] W. Ostwald, Studien Uber Die Bildung und Umwandlung Fester Korper, Zeitschrift Für Phys. Chemie 22 (1897) 289–330.
[60] C.E. Housecroft, A.G. Sharpe, Inorganic Chemistry, 3rd ed., Pearson Education Limited, Harlow, 2008.
[61] V.A. Alves, C.M.A. Brett, A. Cavaleiro, Influence of heat treatment on the corrosion of high speed steel, J. Appl. Electrochem. 31 (2001) 65–72.
[62] Y. Choi, F. Farelas, S. Nešic, Corrosion Behavior of Deep Water Oil Production Tubing Material Under Supercritical CO_2 Environment : Part 1 — Effect of Pressure and Temperature, Corrosion. 70 (2014) 38–47.
[63] M.-W. Tan, E. Akiyama, A. Kawashima, K. Asami, K. Hashimoto, The effect of air exposure on the corrosion behavior of amorphous Fe-8Cr-Mo-13P-7C alloys in 1M HCl, Corros. Sci. 37 (1995) 1289–1301.
[64] M.F. Montemor, A.M.P. Simões, M.G.S. Ferreira, M. Da Cunha Belo, The role of Mo in the chemical composition and semiconductive behaviour of oxide films formed on stainless steels, Corros. Sci. 41 (1999) 17–34.
[65] B. Kinsella, Y.J. Tan, S. Bailey, Electrochemical Impedance Spectroscopy and Surface Characterization Techniques to Study Carbon Dioxide Corrosion Product Scales, Corrosion 54 (1998) 835–842.
[66] A.E. Hughes, J.M. Mol, M.L. Zheludkevich, R.G. Buchheit (Eds.), Active Protective Coatings, VIII, Springer, 2016.
[67] G.V. Karpenko, A.K. Mindyuk, O.P. Savitskaya, Y.I. Babei, Effect of tempering on the corrosion resistance of quench-hardened steel, Fiz. Mekhanika Mater. 6 (1973) 3–6.
[68] W. Li, D.Y. Li, Variations of work function and corrosion behaviors of deformed copper surfaces, Appl. Surf. Sci. 240 (2005) 388–395, https://doi.org/10.1016/j.apsusc.2004.07.017.
[69] E. Rafiee, M. Farzam, M.A. Golozar, A. Ashrafi, An investigation on dislocation density in cold-rolled copper using electrochemical impedance spectroscopy, ISRN Corros. 2013 (2013) 1–6.
[70] D. Dwivedi, K. Lepková, T. Becker, Carbon steel corrosion: a review of key surface properties and characterization methods, RSC Adv. 7 (2017) 4580–4610.
[71] L.Q. Guo, M. Li, X.L. Shi, Y. Yan, X.Y. Li, L.J. Qiao, Effect of annealing temperature on the corrosion behavior of duplex stainless steel studied by in situ techniques, Corros. Sci. 53 (2011) 3733–3741.
[72] M. Miao, J. Pan, T. He, Y. Yan, B.Y. Xia, X. Wang, Molybdenum carbide-based electrocatalysts for hydrogen evolution reaction, Chem. - A Eur. J. 23 (2017) 10947–10961.
[73] X. Peng, L. Hu, L. Wang, X. Zhang, J. Fu, K. Huo, et al., Vanadium carbide nanoparticles encapsulated in graphitic carbon network nanosheets: a high-efficiency electrocatalyst for hydrogen evolution reaction, Nano Energy 26 (2016) 603–609.
[74] C. Wan, B.M. Leonard, Iron-doped molybdenum carbide catalyst with high activity and stability for the hydrogen evolution reaction, Chem. Mater. 27 (2015) 4281–4288.
[75] Clara Escriva-Cerdan, Steve Ooi, Gaurav Joshi, Dataset for "Effect of Tempering Heat Treatment on the CO_2 Corrosion Resistance of Quench-Hardened Cr-Mo Low-Alloy Steels for Oil and Gas Applications" vol.1, (2018), https://doi.org/10.17632/j4vfxfnt9j.1 Mendeley Data.